Supplementary Information Appendix: text, figures, and tables

Early anthropogenic impact on Western Central African rainforests 2,600 y ago

Sediment Core. In January 2014 core B14 was collected in the deepest (105-m-deep) and central part of Lake Barombi from an UWITEC hybrid floating platform using a UWITEC percussion piston coring system. The intact sediment-water interface was collected using a Livingstone piston coring system. The sediment was collected in polycarbonate tubes of 90 mm diameter. The platform was anchored on location during the entire 7 days required to complete coring. To construct a complete sediment sequence, consisting of individual 2-m-long core sections (afterwards cut in 1-m-long sections for air cargo transport), we recovered sediments from three overlapping holes down to 16, 18 and 20.5 m. Based on previous studies of the Lake Barombi sediments (1–4) we focused our analyses on the first 12 m of sediments, which represent the Holocene Epoch. A continuous 11.71-m-long composite sequence was constructed from holes B14-2 and B14-5 after core splitting based on lithological features (Fig. S1). Overlapping core sections were aligned using marker layers, XRF measurements at 1-mm interval and high-resolution photographs acquired at GFZ Potsdam. The Lake Barombi sediments mostly comprise dark olive grey organic rich clays and display micro-laminations as well as whitish siderite laminations, which represent continuous deep lake sedimentation under anoxic conditions (3). Turbidites (n = 76), 2-mm- to 40-cm-thick, are interspersed with the organic rich clays and occur across the entire studied sequence. They comprise massive and sometimes graded dark brown silts often including millimeter- to centimeter-sized terrestrial plant macro-remains and are generally capped by a light brown clay layer. Turbidites may either originate from destabilization of sediments deposited on the lake margins or from high erosion events on the lake catchment. Tephras (n = 8), 2-mm- to 4-mm-thick, were also observed. Event deposits (turbidites and tephras) were excised from the original composite depth scale resulting in an event-free 9.94-m-long depth scale.

Age-model of the Studied Core. A chronology for the sediment deposited in recent centuries was obtained by ^{210}Pb, ^{226}Ra, and ^{137}Cs by direct gamma assay at GEOTOP-UQAM-McGILL laboratory (Montréal, Canada) using Ortec HPGe GWL series well-type, coaxial, low-background intrinsic germanium detectors. On core B14-4-St and using 1-cm increment, ^{210}Pb and ^{226}Ra analyses were performed for the top 22 cm, while ^{137}Cs analyses were performed for the top 7 cm (Fig. S2 and Table S1). Prior to age calculation, a 3-mm-thick turbidite was excised from the depth profile. ^{210}Pb dates were calculated following the procedure described in ref. (5) using 10,000 Monte-Carlo simulations to estimate ^{210}Pb dating uncertainties. The profile of excess ^{210}Pb activity decrease indicates generally stable deep lake sedimentation, which is consistent with previous ^{210}Pb analyses at lower resolution from the deep and central part of Lake Barombi (6). Projecting the ^{137}Cs peak–which potentially records the AD 1963, date of maximum atmospheric weapons testing–to the obtained ^{210}Pb chronology, indicates an age 16 ±8 yr younger than expected. Such an age discrepancy may be related to delayed delivery of ^{137}Cs from the lake catchment area. An alternative chronology could be obtained by correcting the calculated ^{210}Pb

dates using the ^{137}Cs date as a reference point. This would, however, require a major decrease in sedimentation rate after AD 1963, which is not consistent with the relatively constant rhythm of sedimentation as suggested from the invariant thickness of micro-laminations for the top 25 cm of sediments (Fig. S2). Thus, we adopted a ^{210}Pb chronology uncorrected by the results from ^{137}Cs.

^{14}C dates were obtained via accelerator mass spectrometry dating at Poznan Radiocarbon Laboratory, primarily on bulk organic matter, as plant macrofossils were rare throughout the sediment record (Fig. S3 and Table S2). Few plant remains could, however, be dated with ^{14}C and were mostly younger than the paired bulk organic carbon ^{14}C dates from the same depth intervals indicating a contamination with old carbon, ranging from 0 to 380 yr, which is a common feature in African lakes (7). To account for this contamination, we used an age correction involving a simple linear interpolation between the depth intervals at which the old-carbon age offsets could be determined (7).

Based on 21 ^{210}Pb dates and 35 ^{14}C dates (Table S3) we generated an age model for the Lake Barombi sediment record (event-free) using Bayesian approaches, as implemented in the freely available R statistical computing package Bacon v2.2 (8, 9) and using the Southern Hemisphere calibration curve SHCal13 (10). No dates, even those from turbidites, were rejected for a priori reasons. The age-depth model has 95% age confidence ranges of 0.7–100 yr over the period -64–140 cal. yr BP and of 100–380 yr over the period 140–10,500 cal. yr BP.

Organic Geochemical Analyses. Core B14 (event-free) was sampled continuously with contiguous 1-cm slabs for the topmost 25 cm of the sequence and contiguous 5-cm slabs for the rest of the sequence. All samples were prepared and analysed in random sequence during each step of organic geochemical analyses. Sediments were freeze-dried, homogenized, and then extracted using an accelerated solvent extractor (ASE350, Dionex) at University of Potsdam with a dichloromethane/methanol mixture of 9:1 at 100°C and 1500 psi, repeated 3 times. The resulting total lipid extracts were evaporated to dryness using N_2 and then separated over a solid phase extraction on silica gel (0.040–0.063 mesh). The *n*-alkanes were eluted with hexane and were further purified over an activated copper column to remove elemental sulfur and over an $AgNO_3$ column to remove unsaturated hydrocarbons. The identification of individual compounds was performed using an Agilent GC MSD (Agilent 5975C MSD, Agilent 7890A GC) equipped with an additional FID. Compounds were quantified by comparison with an internal standard and standard mixtures of *n*-C_{10}–*n*-C_{40} alkanes. Based on their abundance and purity, *n*-C_{29}, *n*-C_{31}, and *n*-C_{33} alkanes were reliably isotopically analysed. δ^{13}C compositions of *n*-alkanes were measured using a Thermo Trace GC coupled via a GCC combustion interface using a constant oxygen trickle and a nickel wire as catalyst operated at 1000°C to a MAT252 MS at MARUM, University of Bremen. δD compositions of *n*-alkanes were measured using a Thermo Scientific Delta V Plus IRMS coupled to a Trace 1310 GC via an Isolink pyrolysis furnace operated at 1420°C at University of Potsdam. For isotope analyses, every sample was analysed at least in duplicate. δ^{13}C isotope values were measured against calibrated reference CO_2 gas and are reported on the VPDB scale. The mean δ^{13}C standard deviation of all measured samples was 0.1 for the *n*-C_{29}, *n*-C_{31}, and *n*-C_{33} *n*-alkane, respectively. Long-term accuracy and precision was monitored by measuring an external *n*-alkane standard of known isotopic composition (chain length: *n*-C_{16}–*n*-C_{34}; isotope composition -33 to -19‰) every six measurements. Long-term accuracy and precision was <0.1 and 0.3‰, respectively. Correction of δD values to the VSMOW scale was done using a linear regression function derived from the relationship of Mix

A5 (obtained from A. Schimmelmann, Indiana University) measurements and Mix A5 known δD values. Three external standards were measured after every sixth to ninth injection to monitor drift. The H_3^+ factor was determined once a day and had a mean value of 2.41 (n = 25; stdev = 0.2). The mean δD standard deviation of all measured samples was 0.8, 0.7, and 1.1‰ for the *n*-C_{29}, *n*-C_{31}, and *n*-C_{33} *n*-alkane, respectively. $\delta^{13}C$ and δD values are reported as the mean and 1σ of replicate measurements.

***n*-C_{31} Alkane as Biomarker for Terrestrial Higher Plants.** Long-chain odd-numbered *n*-alkanes such as *n*-C_{29}, *n*-C_{31} and *n*-C_{33} predominantly derive from the epicuticular wax coating of terrestrial higher plants (11). $\delta D_{n\text{-}C31}$ and $\delta D_{n\text{-}C33}$ showed similar values, while $\delta D_{n\text{-}C29}$ values appeared generally more negative than the other two homologues (Fig. S4). To infer the potential sources of sedimentary *n*-alkanes that may explain the observed differences in δD between homologues, we used molecular distribution parameters such as the Carbon Preference Index (CPI) calculated as follows:

$$CPI = \frac{[(C_{25}+C_{27}+C_{29}+C_{31})+(C_{27}+C_{29}+C_{31}+C_{33})]}{2\,(C_{26}+C_{28}+C_{30}+C_{32})} \qquad \text{(Eq. 1)}$$

Isotopic offsets between *n*-C_{33} and *n*-C_{29} alkanes ($\Delta_{n\text{-}C33\text{-}n\text{-}C29}$ δD) were negatively correlated with CPI, with larger offsets (of ~20‰) at low CPI (of ~4) and null offset at high CPI (of ~7), probably indicating that, at low CPI, *n*-C_{29} alkanes were additionally influenced by contributions of other source organisms such as aquatic macrophytes (12), bacteria (13), or algae (14, 15). Thus, isotope interpretations were based on the *n*-C_{31} alkane, which was the most abundant long-chain homologue with the most precise isotope measurements, and which we infer to exclusively derive from terrestrial higher plants.

Vegetation Changes Inferred from $\delta^{13}C_{n\text{-}C31}$. Prior interpretation, $\delta^{13}C_{n\text{-}C31}$ values of the last ~160 yr were corrected for variations in atmospheric $\delta^{13}C$ associated with the Suess effect by adding the difference between the atmospheric $\delta^{13}C$ value at the time of *n*-alkane sedimentation (16, 17) and the pre-industrial atmospheric $\delta^{13}C$ value (of -6.4‰; ref. (18)) to the $\delta^{13}C$ value of each *n*-alkane. Sedimentary $\delta^{13}C_{n\text{-}C31}$ values either reflect the large variability in $\delta^{13}C$ values of C_3 plants growing under different relative humidity conditions as found today in Cameroon (19) or reflect changes in the relative contribution of C_3 trees/shrubs and C_4 grasses (20). To provide insights into the drivers of sedimentary $\delta^{13}C_{n\text{-}C31}$ values, we analysed pollen on nine representative samples, which encompassed the complete range of variations in carbon isotopes (Fig. S5). Palynological methods used are described in ref. (21). The higher proportion of grasses (poaceae) corresponded with the higher $\delta^{13}C_{n\text{-}C31}$ values, apart for the most recent sediment sample where a pollen grain of maize (*Zea mays*), a C_4 crop, was found. Pollen of maize have poor dispersal properties (22, 23) and suggest that maize was locally cultivated and may have participated to the recent increase in $\delta^{13}C_{n\text{-}C31}$ values. The magnitude and timing of $\delta^{13}C_{n\text{-}C31}$ changes were in close agreement with the lower resolution record of changes in grass pollen abundance previously analysed on a parallel core (1), supporting our assumption that the sedimentary $\delta^{13}C_{n\text{-}C31}$ signal primarily record vegetation (C_3 versus C_4) changes. Furthermore, the increase in the concentration of *n*-C_{33} alkanes relatively to *n*-C_{29} and *n*-C_{31} alkanes during the LHRC (Fig. S4*A*) is evidence for the contribution of plant waxes derived from C_4 grasses since *n*-C_{33} alkanes are predominately produced by C_4 grasses in tropical Africa (19, 24).

In addition to pollen, the detection in lacustrine sediments of pentacyclic triterpene methyl ethers (PTMEs) specific of C_4 crops such as the miliacin may offer the opportunity to investigate the history of millet cultivation in the study area (25, 26). In Europe miliacin is a marker for millet cultivation because *Panicum miliaceum* was introduced from Asia and other grasses of the subfamily Panicoideae are rare in Central Europe (27). We have not investigated miliacin in the sediments of Lake Barombi, however, for two reasons: (*i*) the African pearl millet belongs to another genus (*Pennisetum*) than the broomcorn millet (*Panicum miliaceum*) cultivated in Europe and (*ii*) in Africa, the genus *Pennisetum* has numerous wild species, which are important constituents of the natural savannahs. Thus, the miliacin in the sediments of Lake Barombi may not originate from millet fields but from the surrounding grasslands.

Hydrological Changes Inferred from $\delta D_{n\text{-}C31}$. Additionally to the isotopic composition of the precipitation, $\delta D_{n\text{-}C31}$ can be influenced by isotopic D-enrichment due to soil evaporation and evapotranspiration as well as by changes in vegetation types and associated plant life forms and photosynthetic pathways (28). For example, reported apparent fractionation (ε) between precipitation and *n*-alkane is -129‰ (standard deviation = 22‰; standard error of the mean = 2‰) for C_3 plants (ε_{C3}; ref. (29)) and -145‰ (standard deviation = 20‰; standard error of the mean = 7‰) for C_4 plants (ε_{C4}; ref. (30)). By using paired $\delta^{13}C_{n\text{-}C31}$ values it is possible to correct for the effect of changing vegetation on $\delta D_{n\text{-}C31}$ values as previously demonstrated (31–35). First, we derived the relative contribution of C_3 plant waxes (f_{C3}) to the sediment from the $\delta^{13}C_{n\text{-}C31}$ values by using a linear binary mixing model with end-member values for C_3 plants ($\delta^{13}C_{C3}$ = -33.8‰; standard deviation = 3.9‰; standard error of the mean = 0.4‰) and C_4 plants ($\delta^{13}C_{C4}$ = -20.1‰; standard deviation = 2.5‰; standard error of the mean = 0.4‰) taken from the "All Africa" compilation of ref. (19) as follows:

$$\delta^{13}C_{n-C31} = (f_{C3})\delta^{13}C_{C3} + (1 - f_{C3})\delta^{13}C_{C4} \qquad \text{(Eq. 2)}$$

Solving for f_{C3} Eq. 2 becomes:

$$f_{C3} = \frac{\delta^{13}C_{n-C31} + \delta^{13}C_{C4}}{\delta^{13}C_{C4} - \delta^{13}C_{C3}} \qquad \text{(Eq. 3)}$$

Second, we estimated sedimentary ε_{corr} as follows:

$$\varepsilon_{corr} = (f_{C3})\varepsilon_{C3} + (1 - f_{C3})\varepsilon_{C4} \qquad \text{(Eq. 4)}$$

Third, we subtracted ε_{corr} from $\delta D_{n\text{-}C31}$ to obtain $\delta D_{n\text{-}C31\text{-}corr}$:

$$\delta D_{n-C31-corr} = \left[\frac{\delta D_{n-C31} + 1000}{\left(\frac{\varepsilon_{corr}}{1000}\right) + 1}\right] - 1000 \qquad \text{(Eq. 5)}$$

We estimate the relative contribution of C_4 plant waxes during the height of the LHRC to be on the order of 20-25% and note that the resulting correction of $\delta D_{n\text{-}C31}$ is rather small (ε_{corr} ranging between -135 and -129‰). The corrected and uncorrected records of $\delta D_{n\text{-}C31}$ are therefore very similar (see Fig. 2).

We note that ε_{C3} and ε_{C4} were derived from the analysis of limited individual plant samples, which resulted in significant spread of their values. Plant physiology, biochemistry, undocumented differences in sampling protocol, and differences in the timing of leaf-wax synthesis may explain the observed large interspecies variability within growth forms and/or photosynthetic pathways (28). On the other hand, lake sediments contain the contribution of plant waxes derived from thousands of individuals representing various species within growth forms and/or photosynthetic pathways and integrating several years or decades of leaf generations. Lake sediments therefore integrate the large interspecies variability within growth forms and/or photosynthetic pathway observed in few individual plants, resulting in much less variability (19, 28, 36). Thus, we decided not to include the uncertainties associated to ε_{C3} and ε_{C4} in our total uncertainty propagation.

Stable isotope ratios in meteoric water in southwestern Cameroon are primarily controlled by the amount of precipitation and the supply of recycled continental moisture to the atmospheric vapour reservoir (37, 38). We interpreted changes in $\delta D_{n\text{-C31-corr}}$ as reflecting changes in the δD of precipitation, with D-enriched isotopic values corresponding to drier conditions and D-depleted values to wetter conditions. We note that both the sedimentary $\delta D_{n\text{-C31}}$ data from Lake Barombi and a marine record (GeoB9501-4) offshore Northwest Africa (39) generally covary on decadal timescales with the instrumental records of mean annual precipitation (Fig. S6).

Sea Surface Temperature Changes in the Gulf of Guinea. SST changes in the Gulf of Guinea were reconstructed at high-resolution from marine core MD03-2707 based on Mg/Ca ratios of planktonic foraminifer *Globigerinoides ruber* (40). While the existing Mg/Ca-based SST estimates suggest relatively warm conditions during the early to mid Holocene, the observed changes were subtle and it was speculated that the contemporaneous low salinity, inferred from Ba/Ca ratios of the same foraminifera, could have further depressed Mg/Ca ratios and hence caused it to underestimate the recorded SST maximum (40) (Fig. S7). We reassessed Mg/Ca-based SST estimates to account for the effect of salinity that was previously not quantified following the procedure described in ref. (41) and included in a computational toolkit (PSU Solver; ref. (42)) coded in MATLAB™ (43), which performs bootstrap Monte-Carlo simulations to constrain the multiple sources of uncertainty associated to such quantitative paleo-temperature reconstructions. In order to account for age uncertainties, we estimated the chronology of core MD03-2707 with the Bacon v2.2 model (8, 9) using the marine calibration curve Marine13 (44).

Mg/Ca of foraminiferal calcite was related to temperature (SST in our case) and salinity (sea surface salinity in our case; SSS) using the established equation in ref. (41):

$$ln\left(\frac{\mathrm{Mg}}{\mathrm{Ca}}\right) = 0.084\ \mathrm{SST} + 0.051\ \mathrm{SSS} - 2.54 \qquad \text{(Eq. 6)}$$

To solve for SST, we used paired $\delta^{18}O$ compositions on the calcite from the same foraminifera ($\delta^{18}O_c$), which are dependent on both calcification temperature and on the $\delta^{18}O$ of seawater ($\delta^{18}O_{sw}$), the latter being related to salinity. Here, we used the "low-light" equation described in ref. (45):

$$\mathrm{SST} = 16.5 - 4.8\ (\delta^{18}\mathrm{O_c} - \delta^{18}\mathrm{O_{sw}} + 0.27) \qquad \text{(Eq. 7)}$$

To relate $\delta^{18}O_{sw}$ to SSS, we used the relationship established for the Gulf of Guinea in ref. (46):

$$\delta^{18}O_{sw} = 0.06.\,SSS - 1.55 \qquad \text{(Eq. 8)}$$

Eqs. 6–8 were simultaneously solved using PSU Solver. Reconstructed SST changes from PSU Solver were warmer and more variable than the reported values (40), displaying a ~2.5°C decrease during the Holocene.

As an alternative approach to solve Eq. 6, we assumed that the Ba/Ca ratios that were measured on the same foraminifera were driven by SSS changes alone, following the relationship established in ref. (40):

$$SSS = -7.47\left(\frac{Ba}{Ca}\right) + 37.45 \qquad \text{(Eq. 9)}$$

Using this alternative approach, reconstructed SST changes from PSU Solver described a similar cooling trend during the Holocene as the approach based on $\delta^{18}O_{sw}$ estimates, however, with a much larger variability of up to ~5°C, which is probably excessive. All PSU Solver outputs (SST and SSS) for the core top agreed with the local instrumental data (47) within error.

Potential changes in precipitation seasonality during the LHRC. Vegetation changes related to the LHRC have also been attributed to a change in the seasonal regime of precipitation (more irregular and stormy) that did not involve a change in the annual amount of precipitation (48, 49). For example, the increase in grass pollen marking the Lake Barombi LHRC was linked to savannah extension in the region resulting from a relatively dry climate, however, the synchronous strong extension of diverse pioneer taxa indicated that a reduction in precipitation was improbable and instead it was concluded that a change in annual distribution of precipitation must have led to the LHRC (1). In addition, the findings of rare charred grains of domesticated pearl millet (*Pennisetum glaucum*) in archaeological excavations in Central Africa (50) were also used in support of a seasonally drier climate during the LHRC (51, 52) since the modern cultivars of pearl millet are adapted to semi-arid conditions with a marked dry season. However, detailed archaeobotanical surveys of the wild flora associated with the findings of this cereal showed the persistence of the rainforests or secondary and disturbed forests without savannahs or even dry forests, suggesting that humans either developed effective cultivation methods to cope with the wet climate or used cultivars better adapted to humid conditions prevalent in the rainforests (53).

Modern climatology compared to the spatial distribution of rainforests in Central Africa can help constraining the climatological preferences of the Guineo-Congolian rainforest biome (Fig. S8). Here, we analysed precipitation amount and precipitation seasonality (shown as coefficient of variation: CV, i.e., the standard deviation of the monthly precipitation expressed as a percentage of the annual mean precipitation) derived from the high spatial resolution (of 30 arc sec) CHELSA data (54) together with the vegetation classes from the Collection 5 MODIS Global Land Cover Type product (www.landcover.org). We found that precipitation amount is highly related to precipitation seasonality in Central Africa (Fig. S8*D*). Overall, high precipitation amount of ~2000 mm yr^{-1} and low CV of ~25 occur near the equator, while low precipitation amount of ~200 mm yr^{-1} and high CV of ~175 occur at 12°N. This relationship breakout in the coastal area bordering the northeasternmost part of the Gulf of Guinea, which represents the domain of the "monsoonal paroxysm" (55), where high amount of precipitation occurs (of up to ~11,500 mm yr^{-1} at Debundscha in Cameroon) with higher seasonality (CV of up to ~75) compared to the equatorial climate. Rainforests thrive under climate conditions with precipitation amount of ~1700 mm yr^{-1} and CV between 20 and 60 that characterize the equatorial climate.

They also dominate the vegetation of the "monsoonal paroxysm" domain, which includes the Lake Barombi region. The latter is characterized by high precipitation amounts (of ~3100 ±450 mm yr^{-1}, see Fig. S8*D*) and a moderate seasonality (CV of ~71 ±3 and 3 to 4 months with less than 100 mm $month^{-1}$). Today, in Central Africa, there is no evidence of climate conditions with both similar (or higher) precipitation amounts and significantly larger seasonality (CV >80) than in the Lake Barombi region. Although positive feedbacks between open tree canopy and fire (natural or human-caused) may substantially expand savannah beyond its climatically prescribed range (56, 57), in Central Africa, optimal climate conditions for "natural" non-rainforest vegetation are centred on precipitation amount of ~1500 mm yr^{-1} and CV of ~75. Our hydrological reconstruction does not support that these conditions were reached at any point during the Holocene at Lake Barombi. Instead, our isotopic data suggest that the LHRC occurred during conditions slightly wetter than today (indicated by the slightly lower $\delta D_{n\text{-C31-corr}}$ values before and during the LHRC compared to today).

Based on the current climatology, a replacement of mature rainforests by a forest-savannah mosaic in the Lake Barombi region would probably require both a significant drop in precipitation amount (of >1000 mm yr^{-1}) and an increase in seasonality (CV >75). These data, together with the absence of any abrupt change in hydroclimate in the Lake Barombi record and in both hydroclimate and SST in marine records from the region during the LHRC (40, 58) suggest that this event was not primarily driven by an increase in the seasonality of precipitation associated with a warming of the nearby ocean.

Human Activity and Population Dynamics in WCA. We compiled published ^{14}C dates from archaeological sites in WCA ranging between 10,400 and 15 ^{14}C yr (Database S1). We removed ^{14}C dates based either on carbonates–possibly affected by carbon reservoir effects–or with associated errors greater than 200 yr. After these quality controls, our compiled database included 1202 ^{14}C dates from 460 individual sites. 93% of the included ^{14}C dates had associated errors lower than 100 yr. ^{14}C dates and associated errors were rounded according to the convention of ref. (59). Prior to calculation of the summed probability distributions (SPDs) and any further statistical analysis, ^{14}C dates were binned to correct for investigator bias and oversampling within sites (60–62). ^{14}C dates were binned in space based on 10-km radii with the ArcGIS 10.2.1 (63) spatial analyst toolbox and in time based on the clustering of the mean ^{14}C yr, using a threshold of 200 yr. ^{14}C dates were calibrated using the southern hemisphere calibration curve SHCal13 (10). ^{14}C calibration and SPDs were computed using the freely available R statistical computing package Bchron (9, 64).

Human activity was inferred from SPDs of ^{14}C dated and/or associated material including the occurrence of *Pennisetum glaucum*, *Elaeis guineensis*, iron metallurgy, and pit features. We assumed that the age of a given associated material is equal to ages of nearby dated material. A significant proportion of ^{14}C dates (~53%) derived from undifferentiated macro charcoals sampled in archaeological excavations and soil profiles. Although natural fires (ignited by lighting) in tropical African forests exist, they are extremely rare (65) and the macro charcoals belowground were found often in association with cultural material such as stone tools, pottery, iron furnace, and charred cultigens (66, 67) suggesting that they primarily resulted from human activity.

Population dynamics were reconstructed for the last 5000 yr from the SPD of ^{14}C dates (samples $n = 1139$; sites $n = 425$) compared against formal statistical models using an hypothesis testing approach introduced in ref. (60), further developed in ref. (61), and provided in R

statistical computing language (9) in ref. (62). Preparative binning resulted in 578-binned ^{14}C dates and 246-binned sites. To assess whether the SPD of ^{14}C dates showed statistically relevant fluctuations, we compared SPD distribution against an exponential model (based on 10,000 Monte-Carlo simulations) used as a conservative null hypothesis reflecting long-term preindustrial human population growth and taphonomic processes (60). This method solves numerous biases related to sampling error and fluctuations in the calibration curve (60). Significant (negative or positive) deviations of the SPD reflect changes in the population dynamics that were significantly stronger compared to other periods, although, we refrain from interpreting those deviations in term of absolute population density changes.

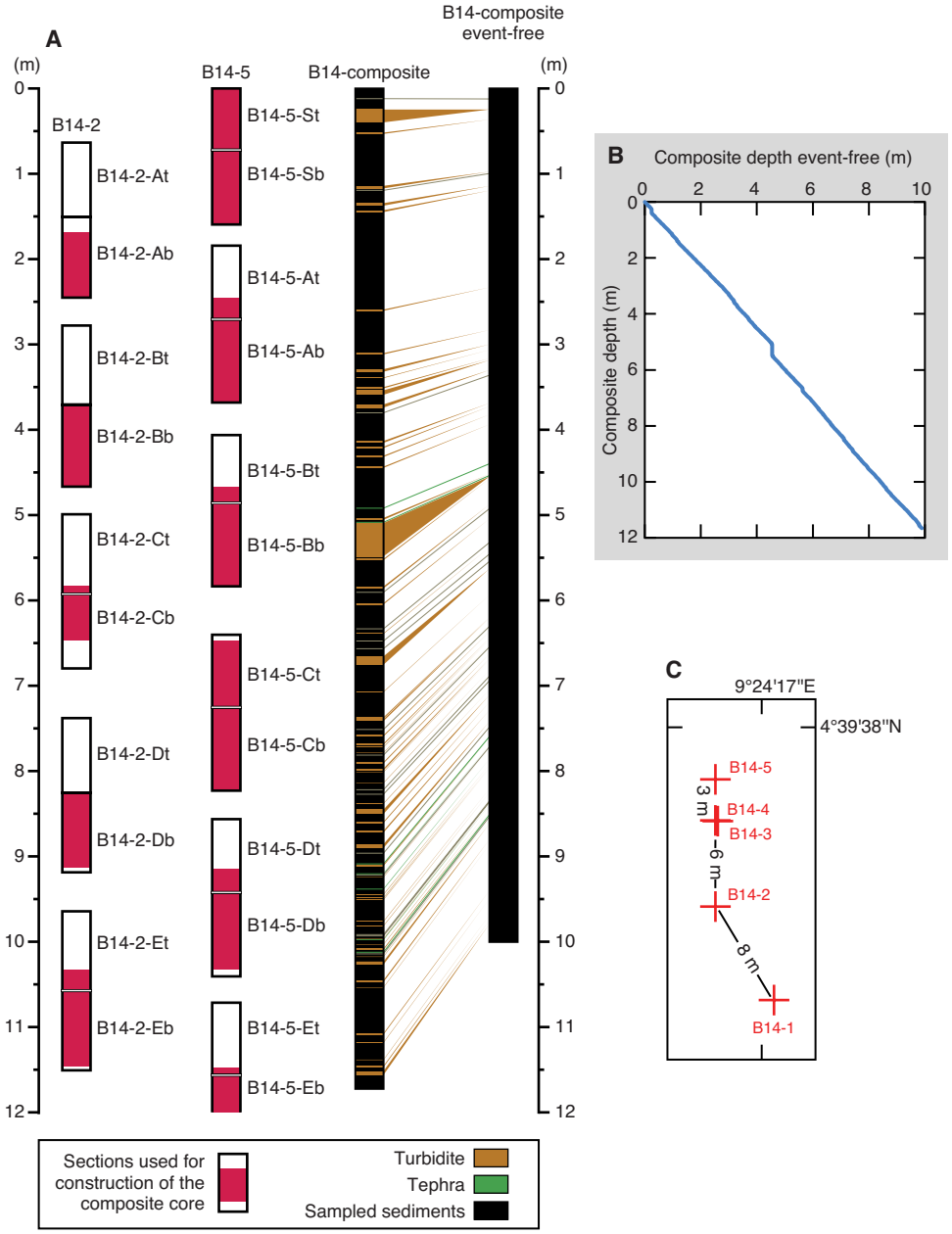

Fig. S1. Lake Barombi core stratigraphy framework. (*A*) Individual core sections used for construction of the composite core of Lake Barombi sediments from the two parallel holes (B14-2 and B14-5). Also shown is the resulting composite core with simplified stratigraphy and composite core event-free. (*B*) Relationship between the original composite depth and the modified composite depth event-free. (*C*) Location map of the sediment cores retrieved in January 2014.

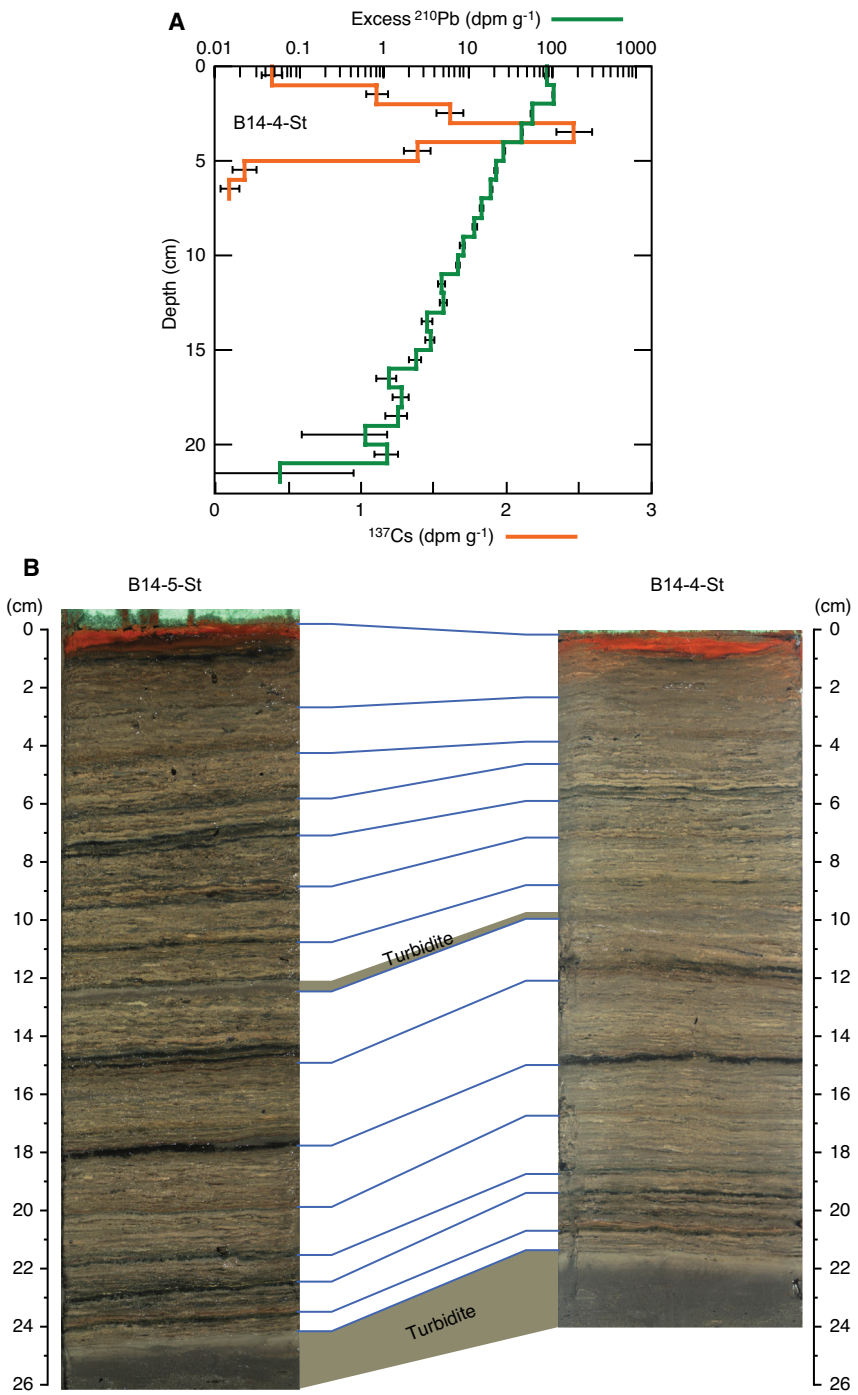

Fig. S2. Radionuclide profiles and lithology of Lake Barombi cores. (*A*) Excess ^{210}Pb and ^{137}Cs activity profiles from core B14-4-St. Error bars represent the 1σ uncertainty. (*B*) Correlation of core B14-4-St and core B14-5-St based on distinctive stratigraphic markers. Note the predominance of micro-laminations. Core B14-5-St was sampled for organic geochemical analyses.

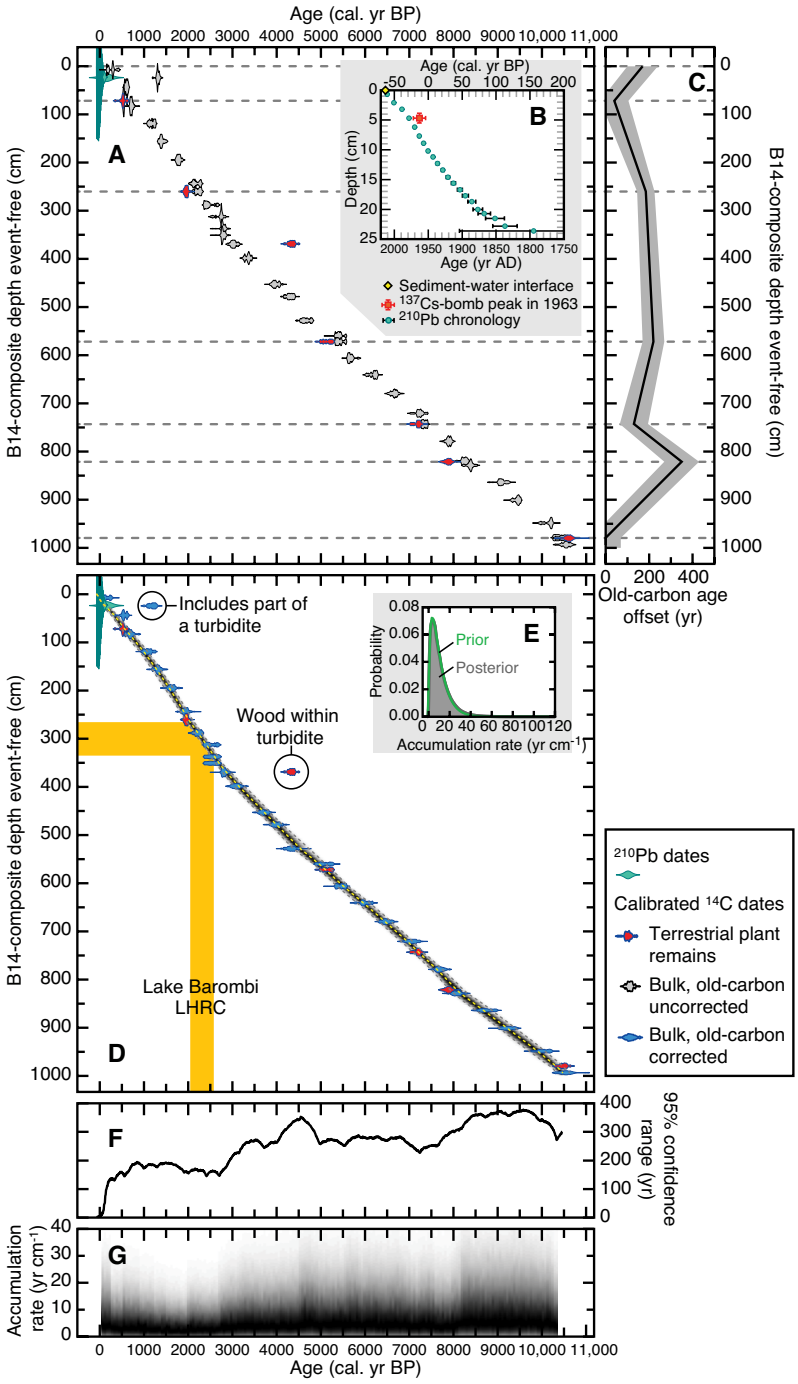

Fig. S3. Age-model of core B14. (*A*) Distribution in time and depth of raw ^{210}Pb and ^{14}C dates. Horizontal dashed lines indicate depth intervals at which old-carbon age offsets could be determined. (*B*) Blow-up of raw ^{210}Pb dates and the potential AD 1963 date based on ^{137}Cs. (*C*) Variation through depth in the old-carbon age offset. Envelopes represent the 1σ uncertainty. (*D*) Posterior age-depth model (grey), overlaying the calibrated distributions of the individual dates calculated using Bacon v2.2 (8). Note that ^{14}C dates on bulk organic carbon were corrected from old-carbon age offsets. Grey dashed lines indicate the model's 95% probability intervals and yellow dashed line indicates the median ages. Horizontal and vertical yellow bands indicate the LHRC depth intervals and timing, respectively. (*E*) Prior and posterior distributions of accumulation rate. (*F*) Variation through time in the width of the 95% confidence ranges. (*G*) Accumulation rate profile; black represents maximum probability, white represents null probability.

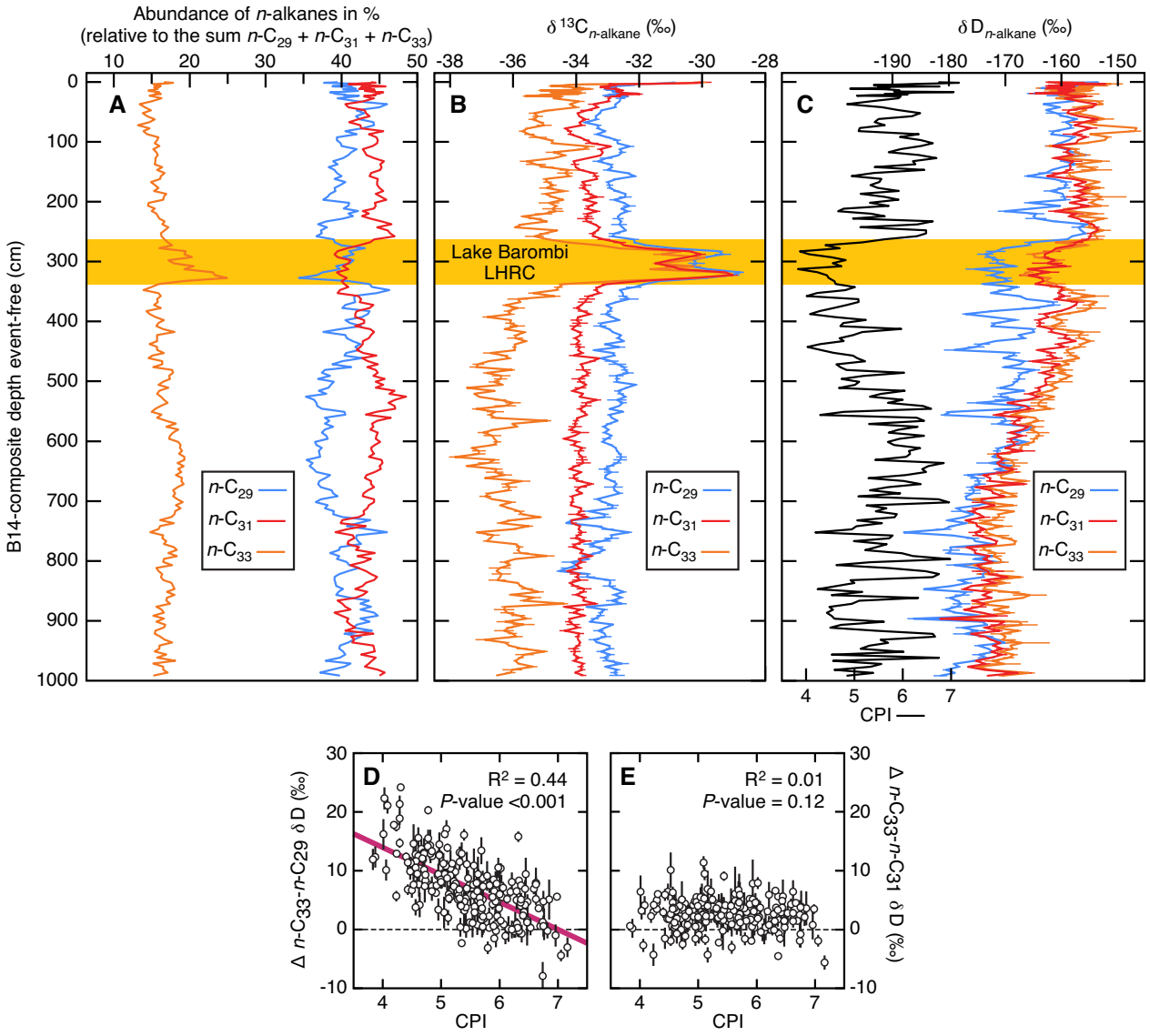

Fig. S4. Relative abundance and carbon and hydrogen isotope compositions of long-chain *n*-alkanes. (*A*) Relative abundance of *n*-C_{29}, *n*-C_{31}, and *n*-C_{33} alkanes. (*B*) $\delta^{13}C$ values of *n*-C_{29}, *n*-C_{31}, and *n*-C_{33} alkanes. (*C*) δD values of *n*-C_{29}, *n*-C_{31}, and *n*-C_{33} alkanes. Also shown is the CPI. Horizontal yellow band indicates the LHRC depth intervals. Error bars based on replicate analyses represent the 1σ uncertainty. (*D*) Relationship between $\Delta_{n\text{-}C33\text{-}n\text{-}C29}$ δD and CPI (significant correlation). (*E*) Relationship between $\Delta_{n\text{-}C33\text{-}n\text{-}C31}$ δD and CPI (no significant correlation).

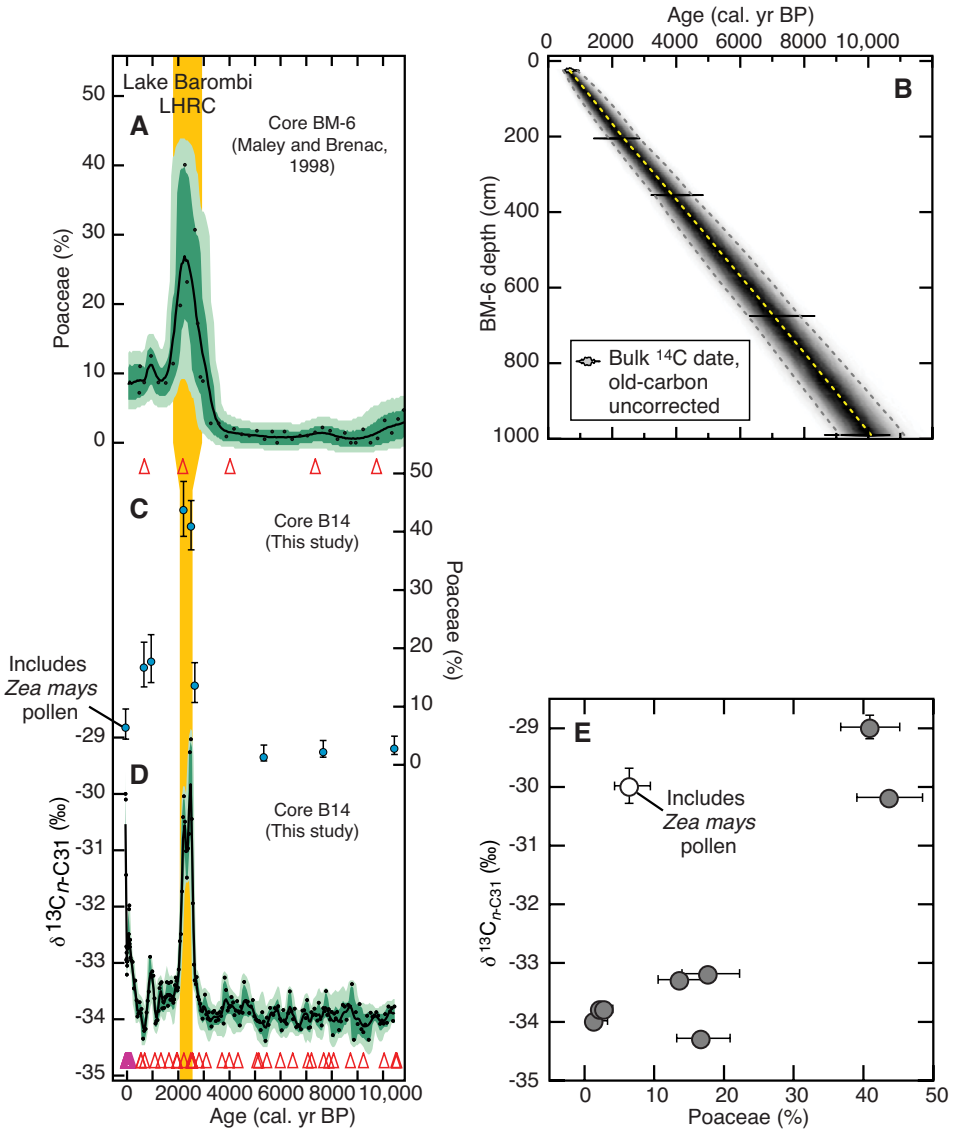

Fig. S5. Comparison between grass pollen abundances and $\delta D_{n\text{-}C31}$ values at Lake Barombi. (*A*) Changes in grass (poaceae) pollen abundance previously analysed on core BM-6 (1). Bottom, red triangles denote ^{14}C used in the core BM-6 age model. (*B*) Posterior age-depth model of core BM-6 (grey), overlaying the calibrated distributions of the individual dates, which was recalculated using Bacon v2.2 (8). The chronology of this core is based on few published dates with large uncertainties; ^{14}C dates were not corrected for old-carbon age offsets and the core depth was not corrected for the presence of event layers. (*C*) Changes in grass pollen abundance on core B14. (*D*) Changes in $\delta^{13}C_{n\text{-}C31}$ values on core B14. $\delta^{13}C_{n\text{-}C31}$ values have been corrected for the Suess effect for the last 160 yr. Bottom, red and purple triangles denote ^{14}C and ^{210}Pb dates, respectively, used in the core B14 age model. (*E*) Scatterplot of $\delta^{13}C_{n\text{-}C31}$ and grass pollen abundance for the core B14. (*A* and *D*) Dots are the raw measured data; lines indicate median probabilities; envelopes reflect 68% (dark) and 95% (light) confidence intervals in the reconstructions, based on analytical and age model errors. (*C* and *E*) Pollen abundance error bars reflect 95% confidence intervals; $\delta^{13}C_{n\text{-}C31}$ error bars reflect the 1σ uncertainty. Vertical yellow band indicates the LHRC timing.

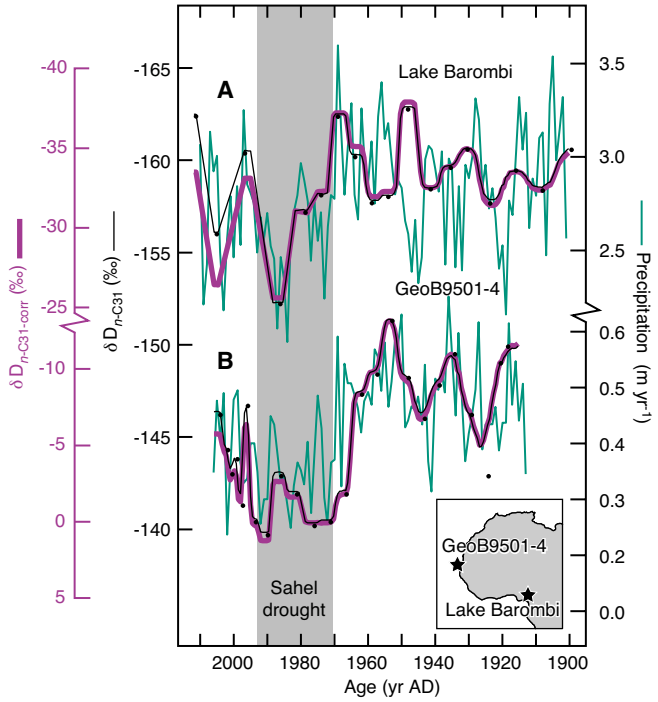

Fig. S6. Relationship between sedimentary $\delta D_{n\text{-C31}}$ and precipitation amount in Central and West Africa. (*A*) $\delta D_{n\text{-C31}}$ values from Lake Barombi since AD 1900, overlain on local instrumental data of precipitation derived from the GPCC V7 gridded dataset (68) (grid-cell latitude: 4° 30'–5°N; grid-cell longitude: 9°–9° 30'E). (*B*) $\delta D_{n\text{-C31}}$ values from marine core GeoB9501-4 since AD 1918, overlain on local instrumental data of precipitation (39). Here, the age-depth model of core GeoB9501-4, based on ^{210}Pb dates, was recalculated using Bacon v2.2 (8) and $\delta D_{n\text{-C31-corr}}$ values were derived from $\delta D_{n\text{-C31}}$ values based on their paired $\delta^{13}C_{n\text{-C31}}$ values (further corrected from the Suess effect) by using the same procedure as for the Lake Barombi record. Single data points are denoted as dots; thin black lines indicate median probabilities ($\delta D_{n\text{-C31}}$) and thick purple lines indicate median probabilities corrected for vegetation changes ($\delta D_{n\text{-C31-corr}}$), both reflecting analytical and age model errors. Instrumental data are denoted in green lines. Grey bar indicates the "Sahel drought".

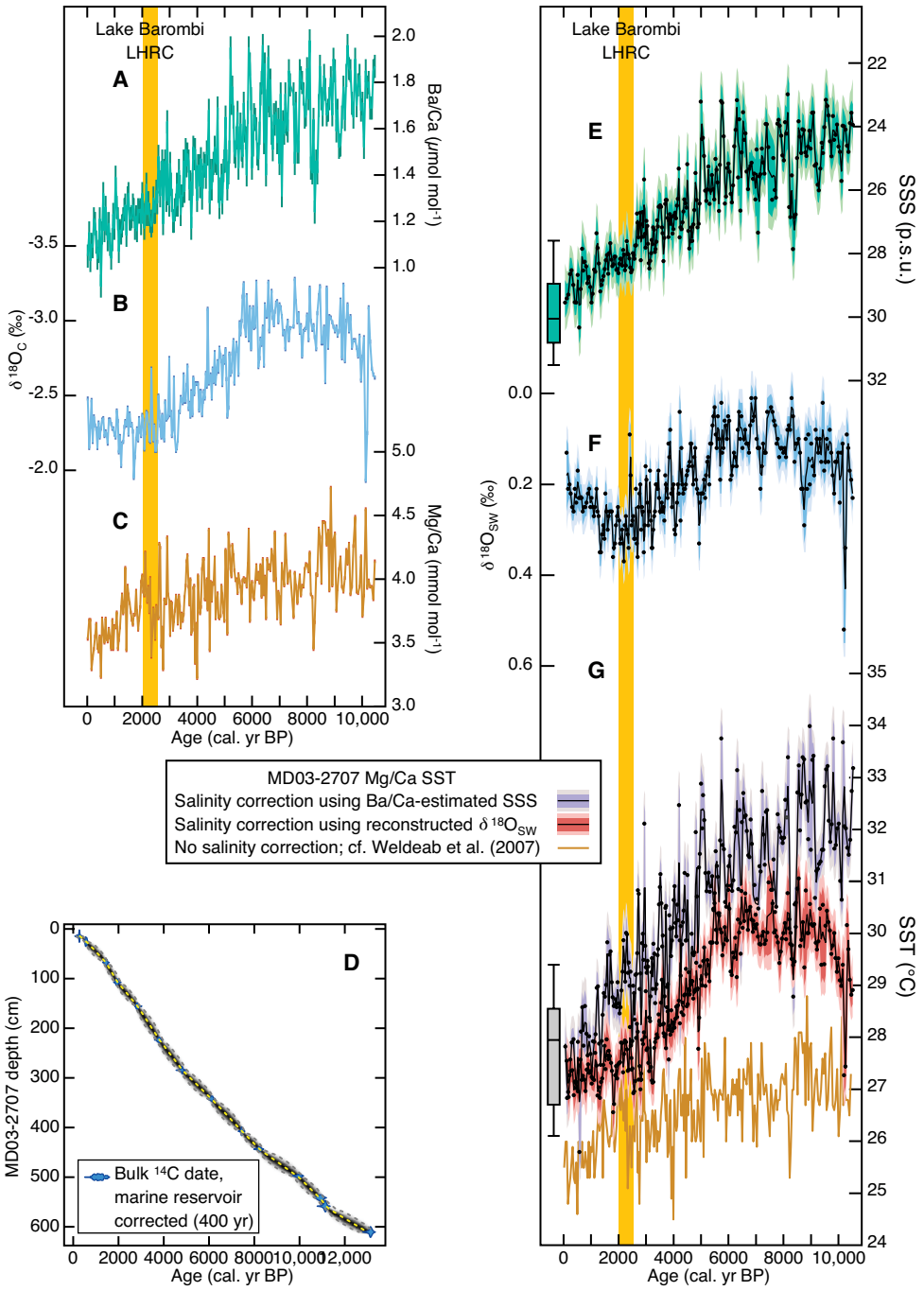

Fig. S7. SST reconstructions from core MD03-2707 in the Gulf of Guinea. (*A*) Ba/Ca in the tests of *G. ruber*, (*B*) $\delta^{18}O_c$, and (*C*) Mg/Ca reported in ref. (40). (*D*) Age-depth model of core MD03-2707 recalculated using Bacon v2.2 (8). Grey dashed lines indicate the model's 95% probability intervals and yellow dashed line indicates the median ages. PSU Solver (42) output (*E–G*). (*E*) Reconstructed Ba/Ca-based SSS. (*F*) Reconstructed $\delta^{18}O_c$-based $\delta^{18}O_{SW}$. (G) Reconstructed Mg/Ca-based SST without salinity correction, corrected from salinity changes using reconstructed $\delta^{18}O_c$-based $\delta^{18}O_{SW}$ and corrected from salinity changes using reconstructed Ba/Ca-based SSS. The box-plots indicate monthly modern SSS (*E*) and SST (*G*) values at the core site (47) (boxes show the median, 25th and 75th percentiles; error bars are extended to extreme data points). (*E–G*) Single data points are denoted as dots; black lines indicate median probabilities; envelopes reflect 68% (dark) and 95% (light) confidence intervals in the reconstructions, based on analytical and age model errors. Vertical yellow bands indicate the LHRC timing.

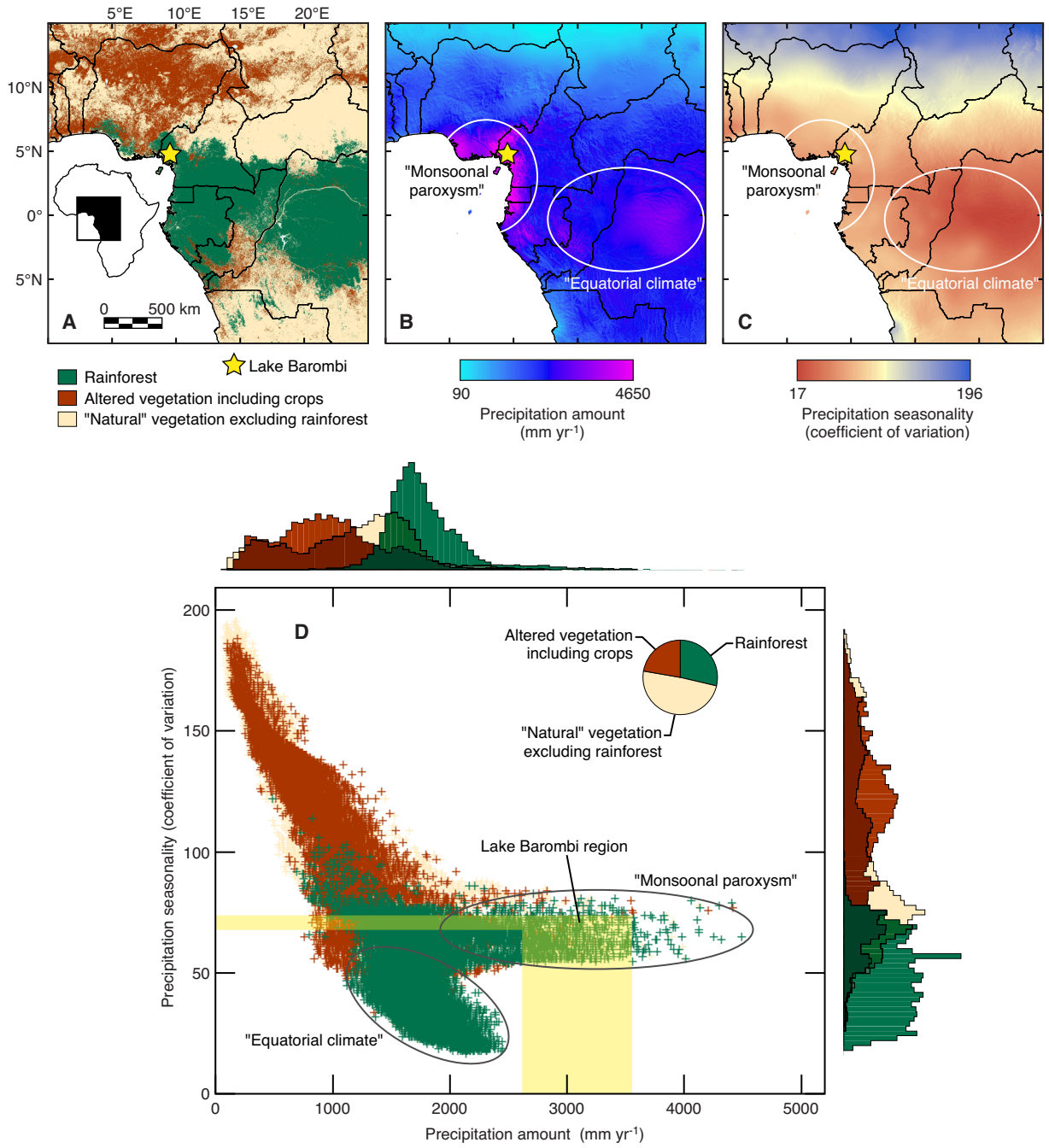

Fig. S8. Current Central African vegetation cover compared to regional climatologies. (*A*) Vegetation cover distribution taken from the Collection 5 MODIS Global Land Cover Type product (www.landcover.org). Rainforest (class "Evergreen Broadleaf Forest") shown in green; Altered vegetation (including classes "Croplands" and "Cropland and Natural Vegetation Mosaic") shown in brown; "Natural" vegetation excluding rainforest (remaining vegetation classes) shown in beige. (*B*) and (*C*) Precipitation amount and seasonality (coefficient of variation), respectively, derived from the CHELSA data (54). (*D*) Precipitation amount versus seasonality. The relative contribution of each vegetation classes to the total vegetation cover is shown as a pie chart at top right hand corner of the scatterplot. Top and right histograms display the relative frequency distribution within each vegetation classes against precipitation amount and seasonality, respectively (the bin size was taken equal for each of the vegetation classes against each respective climatologies). Yellow bands indicate climatologies (1σ estimates) of the Lake Barombi region (i.e., within a radius of 20 km from the lake).

Table S1. ^{210}Pb and ^{137}Cs dataset of the investigated sediment core.

Core B14-4-St interval (cm)	Core B14-4-St depth interval, event-free (cm)	Core B14-4-St mean depth, event-free (cm)	Composite depth event-free (cm)	Cumulative dry mass (g cm^{-2})	^{210}Pb ±1σ (dpm g^{-1})	^{226}Ra ±1σ (dpm g^{-1})	Excess ^{210}Pb ±1σ (dpm g^{-1})	^{210}Pb Age (yr AD)	Age uncertainty (yr)	Sedimentation rate (g cm^{-2} yr^{-1})	Sedimentation rate (cm yr^{-1})	^{137}Cs ±1σ (dpm g^{-1})
0-1	0-1	0.5	0.7	0.0909	89.712 ±2.008	0.972 ±0.192	88.74 ±2.019	2010.6	0.2	0.0262	0.1443	0.383 ±0.074
1-2	1-2	1.5	2.1	0.285	108.817 ±2.347	0.984 ±0.171	107.833 ±2.351	2000.6	0.3	0.0161	0.0779	1.107 ±0.077
2-3	2-3	2.5	3.2	0.494	60.891 ±1.393	1.408 ±0.14	59.484 ±1.4	1988.8	0.4	0.02	0.0942	1.61 ±0.093
3-4	3-4	3.5	4.7	0.6943	46.703 ±1.152	1.494 ±0.247	45.209 ±1.179	1978.4	0.5	0.019	0.1006	2.543 ±0.161
4-5	4-5	4.5	6.2	0.8681	29.34 ±0.803	1.518 ±0.16	27.822 ±0.82	1970	0.7	0.0236	0.1485	1.388 ±0.089
5-6	5-6	5.5	7.7	1.0259	23.544 ±0.803	1.171 ±0.289	22.372 ±0.853	1963.3	0.8	0.0238	0.152	0.199 ±0.082
6-7	6-7	6.5	8.9	1.1745	20.859 ±0.669	1.228 ±0.136	19.632 ±0.682	1956.8	1	0.0222	0.1576	0.095 ±0.066
7-8	7-8	7.5	10.2	1.3247	16.83 ±0.746	1.475 ±0.193	15.355 ±0.773	1950.2	1.2	0.023	0.1442	
8-9	8-9	8.5	11.2	1.4874	13.894 ±0.732	1.316 ±0.11	12.578 ±0.741	1943	1.4	0.0225	0.136	
9-10	9-9.8	9.4	12.3	1.6459	10.315 ±0.527	1.328 ±0.054	8.987 ±0.529	1936.3	1.6	0.0255	0.1347	
10-11	9.8-10.8	10.3	13.4	1.8287	9.408 ±0.471	1.371 ±0.111	8.037 ±0.484	1928.6	2	0.0226	0.1054	
11-12	10.8-11.8	11.3	14.6	2.0148	6.356 ±0.443	1.264 ±0.171	5.092 ±0.475	1921	2.4	0.0279	0.1762	
12-13	11.8-12.8	12.3	15.6	2.2032	6.831 ±0.403	1.434 ±0.225	5.397 ±0.462	1912.8	3	0.0206	0.0941	
13-14	12.8-13.8	13.3	16.7	2.4072	5.151 ±0.438	1.641 ±0.109	3.51 ±0.451	1903.3	3.7	0.0234	0.1238	
14-15	13.8-14.8	14.3	17.7	2.5691	4.797 ±0.41	1.051 ±0.089	3.745 ±0.42	1895.3	4.5	0.0171	0.127	
15-16	14.8-15.8	15.3	18.7	2.7407	4.156 ±0.348	1.606 ±0.134	2.55 ±0.373	1885.8	5.8	0.0188	0.0901	
16-17	15.8-16.8	16.3	20	2.9427	2.868 ±0.261	1.632 ±0.154	1.236 ±0.303	1876.8	7.1	0.029	0.1484	
17-18	16.8-17.8	17.3	20.7	3.1312	3.377 ±0.34	1.626 ±0.067	1.751 ±0.346	1867.5	9.2	0.0155	0.0853	
18-19	17.8-18.8	18.3	21.5	3.3256	2.872 ±0.352	1.291 ±0.214	1.581 ±0.411	1851.6	13.9	0.0108	0.0521	
19-20	18.8-19.8	19.3	22.8	3.5009	2.028 ±0.413	1.339 ±0.291	0.688 ±0.505	1836.9	18	0.0151	0.1055	
20-21	19.8-20.8	20.3	23.6	3.6786	2.562 ±0.294	1.351 ±0.213	1.211 ±0.362	1794.8	109.3	0.004	0.0189	
21-22	20.8-21.8	21.3	24.6	3.9068	1.528 ±0.332	1.415 ±0.186	0.113 ±0.381					

Table S2. Old-carbon age offsets estimated in the investigated sediment core.

Lab ID or sediment marker	Material	Composite depth, event-free (cm)[a]	^{14}C age (yr BP)	Error	Old-carbon age offset (yr)
Marker-1	Undisturbed sediment-water interface	0	–	–	170 ±70[b]
Poz-67632	Bulk sediment	0.5	modern; $F^{14}C$ = 1.0694	$F^{14}C$ error = 0.0033	
Poz-74026	Bulk sediment	71.9	580	30	40 ±65
Poz-67636	Rootlets	71.9	540	60	
Poz-74027	Bulk sediment	260.3	2225	30	185 ±40
Poz-67635	Charcoal	260.3	2040	30	
Poz-74028	Bulk sediment	571.9	4730	35	220 ±50
Poz-67646	Charcoal	571.9	4510	35	
Poz-67653	Charcoal	743	6310	50	
Poz-74029	Bulk sediment	743.2	6440	40	130 ±65
Poz-74030	Bulk sediment	820.1	7450	40	
Poz-67666	Plant remains	818.3-824.3	7100	70	350 ±80
Poz-77991	Bulk sediment	978.9	9230	50	
Poz-77988	Plant remains[c]	977.1-981.7	9340	50	0 (-15) ±70[d]
Poz-77990	Bulk sediment	979.9	9420	50	

[a]Apart for samples Poz-67666 and Poz-77988 where sampled depths are given as ranges, ^{14}C dates are from 1-cm-thick sediment slices and the given depths are their mid-points.
[b]Old-carbon age offset calculated according to ref. (69) using the $F^{14}C$ of the modern sample and the atmospheric $F^{14}C$ encompassing years 2008 to 2013 (corresponding to the age of the ^{14}C-dated sample according to the ^{210}Pb chronology). Atmospheric $F^{14}C$ was derived from the Levin dataset (70, 71) as it includes measurements through year 2016.
[c]Plant remains found in a turbidite.
[d]Old-carbon age offset calculated from the ^{14}C age difference between plant remains in turbidite and bulk-organic carbon sampled directly above and below this event layer. The resulting offset was small but negative (-15 yr) and was rounded to 0 yr.

Table S3. ^{14}C dataset of the investigated sediment core used for the age-depth model.

Lab ID	Material	Composite depth, event-free (cm)	^{14}C age (yr BP)	^{14}C age error (yr)	Old-carbon age offset (yr)
Poz-74025	Bulk sediment	7.5	270	30	155 ±70
Poz-67633	Bulk sediment	24.2	1450	30	125 ±70
Poz-67661	Bulk sediment	43.8	665	30	90 ±65
Poz-67636	Rootlets	71.9	540	60	
Poz-67662	Bulk sediment	82.9	845	30	50 ±65
Poz-67663	Bulk sediment	119.1	1295	30	75 ±60
Poz-67664	Bulk sediment	156	1555	30	105 ±55
Poz-67665	Bulk sediment	194.7	1890	30	135 ±50
Poz-67634	Bulk sediment	243.8	2195	30	170 ±40
Poz-67635	Charcoal	260.3	2040	30	
Poz-77986	Bulk sediment	288.1	2435	30	190 ±40
Poz-67637	Bulk sediment	312.6	2655	30	190 ±40
Poz-77987	Bulk sediment	337.4	2705	35	195 ±40
Poz-67638	Bulk sediment	350.9	2705	35	195 ±45
Poz-67640	Plant remains	367.7-370.1	3950	40	
Poz-74031	Bulk sediment	369.6	2935	30	195 ±45
Poz-67641	Bulk sediment	398.5	3180	30	200 ±45
Poz-67642	Bulk sediment	452.9	3690	35	205 ±45
Poz-67643	Bulk sediment	478.4	3915	35	210 ±45
Poz-67644	Bulk sediment	528.2	4165	35	215 ±50
Poz-67647	Bulk sediment	560.1	4705	35	220 ±50
Poz-67646	Charcoal	571.9	4510	35	
Poz-67648	Bulk sediment	606.2	4970	40	200 ±55
Poz-67650	Bulk sediment	640.8	5440	40	185 ±55
Poz-67651	Bulk sediment	679.7	5890	40	165 ±60
Poz-67652	Bulk sediment	720.7	6350	50	140 ±65
Poz-67653	Charcoal	743	6310	50	
Poz-67654	Bulk sediment	778.8	7110	40	230 ±70
Poz-67666	Plant remains	818.3-824.3	7100	70	
Poz-67655	Bulk sediment	828.7	7620	50	335 ±80
Poz-67656	Bulk sediment	863.8	8180	50	255 ±75
Poz-67657	Bulk sediment	901	8470	50	175 ±75
Poz-67658	Bulk sediment	948.5	9060	50	70 ±70
Poz-77988	Plant remains	977.1-981.7	9340	50	
Poz-67660	Bulk sediment	993.4	9380	50	0 ±70

[a]Apart for samples Poz-67640, Poz-67666, and Poz-77988 where sampled depths are given as ranges, ^{14}C dates are from 1-cm-thick sediment slices and the given depths are their mid-points.

1. Maley J, Brenac P (1998) Vegetation dynamics, palaeoenvironments and climatic changes in the forests of western Cameroon during the last 28,000 years BP. *Rev. Palaeobot. Palynol.* 99:157–187.
2. Giresse P, Maley J, Brenac P (1994) Late Quaternary palaeoenvironments in the Lake Barombi Mbo (West Cameroon) deduced from pollen and carbon isotopes of organic matter. *Palaeogeogr. Palaeoclimatol. Palaeoecol.* 107:65–78.
3. Giresse P, Maley J, Kelts K (1991) Sedimentation and palaeoenvironment in crater lake Barombi Mbo, Cameroon, during the last 25,000 years. *Sediment. Geol.* 71:151–175.
4. Cornen G, Bande Y, Giresse P, Maley J (1992) The nature and chronostratigraphy of Quaternary pyroclastic accumulations from lake Barombi Mbo (West-Cameroon). *J. Volcanol. Geotherm. Res.* 51:357–374.
5. Sanchez-Cabeza J-A, Ruiz-Fernández AC, Ontiveros-Cuadras JF, Pérez Bernal LH, Olid C (2014) Monte Carlo uncertainty calculation of ^{210}Pb chronologies and accumulation rates of sediments and peat bogs. *Quat. Geochronol.* 23:80–93.
6. Giresse P, Ngos S, Pourchet M (1994) Processus sédimentaires séculaires et géochronologie au ^{210}Pb des principaux lacs de la dorsale camerounaise. *Bull. Soc. Géol. Fr.* 165:363–380.
7. Blaauw M, *et al.* (2011) High-resolution ^{14}C dating of a 25,000-year lake-sediment record from equatorial East Africa. *Quat. Sci. Rev.* 30:3043–3059.
8. Blaauw M, Christen JA (2011) Flexible paleoclimate age-depth models using an autoregressive gamma process. *Bayesian Anal.* 6:457–474.
9. R Development Core Team (2016) R: A Language and Environment for Statistical Computing (R Foundation for Statistical Computing, Vienna, Austria).
10. Hogg AG, *et al.* (2013) SHCal13 Southern Hemisphere Calibration, 0–50,000 Years cal BP. *Radiocarbon* 55:1889–1903.
11. Eglinton G, Hamilton RJ (1967) Leaf Epicuticular Waxes. *Science* 156:1322–1334.
12. Aichner B, Herzschuh U, Wilkes H (2010) Influence of aquatic macrophytes on the stable carbon isotopic signatures of sedimentary organic matter in lakes on the Tibetan Plateau. *Org. Geochem.* 41:706–718.
13. Han J, Calvin M (1969) Hydrocarbon distribution of algae and bacteria, and microbiological activity in sediments. *Proc. Natl. Acad. Sci. U.S.A.* 64:436–443.
14. Lichtfouse É, Derenne S, Mariotti A, Largeau C (1994) Possible algal origin of long chain odd *n*-alkanes in immature sediments as revealed by distributions and carbon isotope ratios. *Org. Geochem.* 22:1023–1027.
15. Gelpi E, Schneider H, Mann J, Oró J (1970) Lipids of Geochemical Significance in Microscopic Algae, Part I: Hydrocarbons of Geochemical Significance in Microscopic Algae. *Phytochemistry* 9:603–612.
16. Francey RJ, *et al.* (1999) A 1000-year high precision record of δ^{13}C in atmospheric CO_2. *Tellus* 51:170–193.
17. Keeling RF, Piper SC, Bollenbacher AF, Walker SJ (2010) Monthly atmospheric ^{13}C/^{12}C isotopic ratios for 11 SIO stations. in *Trends: A Compendium of Data on Global Change* (Carbon Dioxide Information Analysis Center, Oak Ridge National Laboratory, U.S. Department of Energy, Oak Ridge, Tenn., U.S.A.).
18. McCarroll D, Loader NJ (2004) Stable isotopes in tree rings. *Quat. Sci. Rev.* 23:771–801.
19. Garcin Y, *et al.* (2014) Reconstructing C_3 and C_4 vegetation cover using *n*-alkane carbon isotope ratios in recent lake sediments from Cameroon, Western Central Africa. *Geochim. Cosmochim. Acta* 142:482–500.
20. Castañeda IS, *et al.* (2009) Wet phases in the Sahara/Sahel region and human migration patterns in North Africa. *Proc. Natl. Acad. Sci. U.S.A.* 106:20159–20163.
21. Dupont LM, Linder HP, Rommerskirchen F, Schefuß E (2011) Climate-driven rampant speciation of the Cape flora. *J. Biogeogr.* 38:1059–1068.
22. Raynor GS, Ogden EC, Hayes JV (1972) Dispersion and Deposition of Corn Pollen from Experimental Sources. *Agron. J.* 64:420–427.
23. Lane CS, Cummings KE, Clark JJ (2010) Maize pollen deposition in modern lake sediments: A case study from Northeastern Wisconsin. *Rev. Palaeobot. Palynol.* 159:177–187.
24. Rommerskirchen F, Plader A, Eglinton G, Chikaraishi Y, Rullkötter J (2006) Chemotaxonomic significance of distribution and stable carbon isotopic composition of long-chain alkanes and alkan-1-ols in C_4 grass waxes. *Org. Geochem.* 37:1303–1332.
25. Schwab VF, *et al.* (2015) Effect of aridity on δ^{13}C and δD values of C_3 plant- and C_4 graminoid-derived leaf wax lipids from soils along an environmental gradient in Cameroon (Western Central Africa). *Org. Geochem.* 78:99–109.
26. Bossard N, *et al.* (2013) Distribution of miliacin (olean-18-en-3β-ol methyl ether) and related compounds in broomcorn millet (*Panicum miliaceum*) and other reputed sources: Implications for the use of sedimentary miliacin as a tracer of millet. *Org. Geochem.* 63:48–55.

27. Jacob J, *et al*. (2008) Millet cultivation history in the French Alps as evidenced by a sedimentary molecule. *J. Archaeol. Sci*. 35:814–820.
28. Sachse D, *et al*. (2012) Molecular Paleohydrology: Interpreting the Hydrogen-Isotopic Composition of Lipid Biomarkers from Photosynthesizing Organisms. *Annu. Rev. Earth Planet. Sci*. 40:221–249.
29. Feakins SJ, *et al*. (2016) Plant leaf wax biomarkers capture gradients in hydrogen isotopes of precipitation from the Andes and Amazon. *Geochim. Cosmochim. Acta* 182:155–172.
30. Smith FA, Freeman KH (2006) Influence of physiology and climate on δD of leaf wax *n*-alkanes from C_3 and C_4 grasses. *Geochim. Cosmochim. Acta* 70:1172–1187.
31. Collins JA, *et al*. (2013) Estimating the hydrogen isotopic composition of past precipitation using leaf-waxes from western Africa. *Quat. Sci. Rev*. 65:88–101.
32. Feakins SJ (2013) Pollen-corrected leaf wax D/H reconstructions of northeast African hydrological changes during the late Miocene. *Palaeogeogr. Palaeoclimatol. Palaeoecol*. 374:62–71.
33. Magill CR, Ashley GM, Freeman KH (2013) Water, plants, and early human habitats in eastern Africa. *Proc. Natl. Acad. Sci. U.S.A*. 110:1175–1180.
34. Shanahan TM, *et al*. (2015) The time-transgressive termination of the African Humid Period. *Nat. Geosci*. 8:140–144.
35. Tierney JE, Pausata FSR, deMenocal PB (2017) Rainfall regimes of the Green Sahara. *Sci. Adv*. 3:e1601503.
36. Sachse D, Radke J, Gleixner G (2006) δD values of individual *n*-alkanes from terrestrial plants along a climatic gradient – Implications for the sedimentary biomarker record. *Org. Geochem*. 37:469–483.
37. Njitchoua R, *et al*. (1999) Variations of the stable isotopic compositions of rainfall events from the Cameroon rain forest, Central Africa. *J. Hydrol*. 223:17–26.
38. Wirmvem MJ, *et al*. (2016) Variation in stable isotope ratios of monthly rainfall in the Douala and Yaounde cities, Cameroon: local meteoric lines and relationship to regional precipitation cycle. *Appl. Water Sci*., doi:10.1007/s13201-016-0413-4.
39. Niedermeyer EM, *et al*. (2016) The stable hydrogen isotopic composition of sedimentary plant waxes as quantitative proxy for rainfall in the West African Sahel. *Geochim. Cosmochim. Acta* 184:55–70.
40. Weldeab S, Lea DW, Schneider RR, Andersen N (2007) Centennial scale climate instabilities in a wet early Holocene West African monsoon. *Geophys. Res. Lett*. 34:L24702.
41. Tierney JE, Pausata FSR, deMenocal P (2016) Deglacial Indian monsoon failure and North Atlantic stadials linked by Indian Ocean surface cooling. *Nat. Geosci*. 9:46–50.
42. Thirumalai K, Quinn TM, Marino G (2016) Constraining past seawater $\delta^{18}O$ and temperature records developed from foraminiferal geochemistry. *Paleoceanography* 31:1409–1422.
43. MATLAB and Statistics Toolbox Release 2015a (The MathWorks, Inc., Natick, MA).
44. Reimer PJ, *et al*. (2013) IntCal13 and Marine13 Radiocarbon Age Calibration Curves 0–50,000 Years cal BP. *Radiocarbon* 55:1869–1887.
45. Bemis BE, Spero HJ, Bijma J, Lea DW (1998) Reevaluation of the oxygen isotopic composition of planktonic foraminifera: Experimental results and revised paleotemperature equations. *Paleoceanography* 13:150–160.
46. Leduc G, Sachs JP, Kawka OE, Schneider RR (2013) Holocene changes in eastern equatorial Atlantic salinity as estimated by water isotopologues. *Earth Planet. Sci. Lett*. 362:151–162.
47. Levitus S, Boyer T (1994) World Ocean Atlas 1994, Temperature (National Oceanic and Atmospheric Administration, National Environmental Satellite, Data, and Information Service, US Department of Commerce, Washington, DC).
48. Maley J (2002) A Catastrophic Destruction of African Forests about 2,500 Years Ago Still Exerts a Major Influence on Present Vegetation Formations. *IDS Bull*. 30:13–30.
49. Maley J, Giresse P, Doumenge C, Favier C (2012) Comment on "Intensifying Weathering and Land Use in Iron Age Central Africa". *Science* 337:1040.
50. Eggert MKH, *et al*. (2006) Pits, graves and grains: archaeological and archaeobotanical research in southern Cameroun. *J. Afr. Archaeol*. 4:273–298.
51. Ngomanda A, Neumann K, Schweizer A, Maley J (2009) Seasonality change and the third millennium BP rainforest crisis in southern Cameroon (Central Africa). *Quat. Res*. 71:307–318.
52. Neumann K, *et al*. (2012) First farmers in the Central African rainforest: A view from southern Cameroon. *Quat. Int*. 249:53–62.

53. Kahlheber S, Eggert MKH, Seidensticker D, Wotzka H-P (2014) Pearl Millet and Other Plant Remains from the Early Iron Age Site of Boso-Njafo (Inner Congo Basin, Democratic Republic of the Congo). *Afr. Archaeol. Rev.* 31.
54. Karger DN, *et al.* (2017) Climatologies at high resolution for the earth's land surface areas. *Sci. Data* 4:170122.
55. Suchel JB (1987) Les climats du Cameroun. PhD thesis (Univ. of Bordeaux III, France).
56. Staver AC, Archibald S, Levin SA (2011) The Global Extent and Determinants of Savanna and Forest as Alternative Biome States. *Science* 334:230–232.
57. Aleman JC, Jarzyna MA, Staver AC (2018) Forest extent and deforestation in tropical Africa since 1900. *Nat. Ecol. Evol.* 2:26–33.
58. Collins JA, *et al.* (2017) Rapid termination of the African Humid Period triggered by northern high-latitude cooling. *Nat. Commun.* 8:1372.
59. Stuiver M, Polach HA (1977) Discussion: Reporting of ^{14}C data. *Radiocarbon* 19:355–363.
60. Shennan S, *et al.* (2013) Regional population collapse followed initial agriculture booms in mid-Holocene Europe. *Nat. Commun.* 4:2486.
61. Timpson A, *et al.* (2014) Reconstructing regional population fluctuations in the European Neolithic using radiocarbon dates: a new case-study using an improved method. *J. Archaeol. Sci.* 52:549–557.
62. Crema ER, Habu J, Kobayashi K, Madella M (2016) Summed Probability Distribution of ^{14}C Dates Suggests Regional Divergences in the Population Dynamics of the Jomon Period in Eastern Japan. *PLoS ONE* 11:e0154809.
63. ArcGIS (2010) Version 10 (Redlands CA: Environmental Systems Research Institute Inc.).
64. Parnell A (2015) Bchron: Radiocarbon dating, age-depth modelling, relative sea level rate estimation, and non-parametric phase modelling (R package version 4.1.2).
65. Caroline EGT, Lee JTW, Mackanga-Missandzou A (1996) Lightning Strike Burns Large Forest Tree in the Lopé Reserve, Gabon. *Global Ecol. Biogeogr.* 5:36–41.
66. Morin-Rivat J, *et al.* (2016) High spatial resolution of late-Holocene human activities in the moist forests of central Africa using soil charcoal and charred botanical remains. *The Holocene* 26:1954–1967.
67. Hubau W, *et al.* (2013) Ancient charcoal as a natural archive for paleofire regime and vegetation change in the Mayumbe, Democratic Republic of the Congo. *Quat. Res.* 80:326–340.
68. Schneider U, *et al.* (2015) GPCC Full Data Reanalysis Version 7.0 at 0.5°: monthly land-surface precipitation from rain-gauges built on GTS-based and historic data (Global Precipitation Climatology Centre, doi:10.5676/DWD_GPCC/FD_M_V7_050).
69. Keaveney EM, Reimer PJ (2012) Understanding the variability in freshwater radiocarbon reservoir offsets: a cautionary tale. *J. Archaeol. Sci.* 39:1306–1316.
70. Levin I, Kromer B, Hammer S (2013) Atmospheric $\Delta^{14}CO_2$ trend in Western European background air from 2000 to 2012. *Tellus* 65:20092.
71. Hammer S, Levin I (2017) Monthly mean atmospheric $\Delta^{14}CO_2$ at Jungfraujoch and Schauinsland from 1986 to 2016 (heiDATA Dataverse, V2, doi:10.11588/data/10100).